A nonlinear piezoelectric shunt absorber with 2:1 internal resonance: experimental proof of concept

Zein Alabidin Shami[1], **Christophe Giraud-Audine**[2] **and Olivier Thomas**[1,*]

[1] Arts et Metiers Institute of Technology, LISPEN, HESAM Université, F-59000 Lille, France
[2] Arts et Metiers Institute of Technology, L2EP, HESAM Université, Univ. Lille, Centrale Lille, HEI, F-59000 Lille, France

E-mail: olivier.thomas@ensam.eu

Abstract

An experimental proof of concept of a new semi-passive nonlinear piezoelectric shunt absorber, introduced theoretically in a companion article, is presented in this work. This absorber is obtained by connecting, through a piezoelectric transducer, an elastic structure to a resonant circuit that includes a quadratic nonlinearity. This nonlinearity is obtained by including in the circuit a voltage source proportional to the square of the voltage across the piezoelectric transducer, thanks to an analog multiplier circuit. Then, by tuning the electric resonance of the circuit to half the value of one of the resonances of the elastic structure, a two-to-one internal resonance is at hand. As a result, a strong energy transfer occurs from the mechanical mode to be attenuated to the electrical mode of the shunt, leading to two essential features: a nonlinear antiresonance in place of the mechanical resonance and an amplitude saturation. Namely, the amplitude of the elastic structure oscillations at the antiresonance becomes, above a given threshold, independent of the forcing level, contrary to a classical linear resonant shunt. This paper presents the experimental setup, the designed nonlinear shunt circuit and the main experimental results.

Keywords: nonlinear piezoelectric shunt, vibration attenuation, 2:1 internal resonance, energy transfer, saturation phenomenon

(Some figures may appear in colour only in the online journal)

1. Introduction

Mechanical structures used in industrial applications are often submitted to high levels of vibration. This could lead to large amounts of stress, fatigue, and noise, especially for lightweight structures, reducing their life cycle and the comfort of their users. This article proposes the experimental proof of concept of an original nonlinear piezoelectric shunt vibration absorber, theoretically introduced in [1], and based on an intentional two-to-one internal resonance between a mode of the mechanical structure and a nonlinear electrical oscillator.

Passive dynamical vibrations absorbers were the first to be designed, such as Lanchester [2] or Frahm dampers [3]. They consist of adding inertial, damping, and stiffness components to the primary structure, organized so that their vibrations counteract or dissipate those of the primary structure. Though still well used in many applications, researchers began developing in the early 1990s electromechanical analogs of those mechanical dampers. The principle is to couple the structure vibrations to an electrical circuit thanks to an electromechanical transducer. The circuit, usually called a shunt, can be designed passive, active, or semi-passive in the case

* Author to whom any correspondence should be addressed.

of supplied electronic components such as operational amplifiers. Since piezoelectric transduction was first proposed in the pioneering work [4], electromagnetic transduction has also been investigated (see [5] and reference therein).

Most of the shunts strategies published until now are linear, which means that the electronic circuit is a combination of inductances, resistances, and capacitances, the electric analogs of mechanical inertia, viscous damper, and stiffness. They can be devoted to the resonance reduction of a single mode, with an analog of Frahm and Lanchester dampers (see e.g. [6]), possibly enhanced by negative capacitances [7, 8]. They can also be used to create a frequency adaptive antiresonance to filter a monoharmonic excitation signal [9]. Among others, one can design a shunt with an electronic network as an electromechanical analog of the mechanical structure, to achieve broadband vibration damping (see e.g. [10]). Many other designs have been proposed, the interested reader being redirected to recent review papers on the subject [11, 12].

On the contrary to the above cited linear shunts, nonlinearities can be introduced intentionally in the vibration control device to benefit from particular dynamical phenomena without counterparts in the linear theory. Examples of the use of geometrically nonlinear stiffnesses are reviewed in [13, 14]. Then, in the field of nonlinear absorbers, several strategies have been proposed, that can be gathered in four main families. For each family, the present text considers solutions based on piezoelectric control with experiments, the interested reader being redirected to [1] for a broader literature review. The first family is related to nonlinear energy sinks (NES), which take the benefit of an absorber with strong nonlinearities, into which the energy is transferred and trapped. To our knowledge, only two experimental studies propose a NES that includes a piezoelectric transduction: [15], with an analog electronics that includes multipliers and [16], in an active control philosophy with force feedback. The second family is related to nonlinear tuned vibration absorber (NLTVA), introduced in [17]. They are designed with nonlinearities in the absorber mirroring those of the primary system, leading to self-adaptation to the host structure's dynamics amplitude, contrary to the linear tuned absorbers. Such nonlinear vibration absorbers were extended to piezoelectric shunt circuits theoretically in [18] and experimentally validated in [19–21] with passive electronic components. The third family is related to the so called synchronized switch damping techniques, proposed in [22, 23], that was addressed in many theoretical and experimental studies since (see the recent review [12]).

A fourth family, directly related to our present work, is based on the intentional use of internal resonances. In a nonlinear system, if the ratio of two modal frequencies ω_k and ω_l is a rational number (i.e. $\omega_k/\omega_l \simeq n/m$ with $n,m \in \mathbb{N}^*$), a strong coupling between the two corresponding modes is likely to occur, enabling to transfer energy from one mode to the other. As explained in [1], the present article focus on the intentional use of a 2:1 internal resonance, that is activated by the presence of quadratic nonlinearities in the system, leading to an energy transfer from the driven mode (of natural frequency ω_2), to a mode tuned at half this frequency (of natural frequency $\omega_1 \simeq \omega_2/2$). This leads to two important features: (a) a significant amplitude reduction of the resonance of the driven mode, which is replaced by a nonlinear antiresonance, and (b) a saturation phenomenon, that leads to an amplitude of the driven mode independent of the excitation level. Using the features of a 2:1 internal resonance for vibration reduction purposes has been illustrated in some works in the past, and we focus here only on experimental studies. For example, an analog electronic circuit made of multipliers was proposed in [24, 25] to damp the vibration of a plant composed of a beam connected to the shaft of a DC motor, by tuning the natural frequency of the controller to half that of the beam. In [26], the same technique was used, but with piezoelectric actuators. Moreover, the same method has been applied on different structures like a truss in [27] and triangular panels [28] using a real-time digital controller coupled to the elastic structure with quadratic nonlinearities and tuned to have the saturation phenomenon.

The main originality of our work is to use the particular features of a 2:1 internal resonance in a semi-passive way using a piezoelectric shunt circuit. We proposed a complete theoretical analysis to design such an absorber in a previous work [1], in which a detailed guideline for the absorber design has been given. In this work, an experimental analysis based on the previous theoretical results is proposed, by applying the vibration absorber to a cantilever beam structure to damp its first bending mode. The outline of this paper is as follows: in section 2, a brief theoretical analysis, emphasizing the main features of the designed absorber, is given. In section 3, the experimental setup and protocol, in addition to the nonlinear shunt circuit design, are shown. Finally, section 4 is devoted to experimental results and the absorber's performance.

2. Theory

2.1. Governing equations

In this section, a summary of the main equations that govern the electromechanical system is illustrated. The full theoretical model with numerical and analytical results is outlined in our previous paper [1], and only the main points are recalled here. We consider an arbitrary elastic structure subjected to an external excitation and connected to a nonlinear shunt circuit via a piezoelectric (PE) patch as shown in figure 1. The displacement vector $\boldsymbol{u}(\boldsymbol{x},t)$ at any point $\boldsymbol{x}$ of the structure at date t is expanded on a given linear modes $\phi_i(\boldsymbol{x})$ of the structure in short circuit. One obtains:

$$\boldsymbol{u}(\boldsymbol{x},t) = \phi_i(\boldsymbol{x}) q_i(t), \tag{1}$$

where $q_i(t)$ is the ith modal coordinate, that verifies [1]:

$$\ddot{q}_i + 2\xi_i\hat{\omega}_i\dot{q}_i + \hat{\omega}_i^2 q_i + \frac{\theta_i}{m_i C_{pi}} Q = \frac{F_i}{m_i}\cos\Omega t, \tag{2a}$$

$$\ddot{Q} + 2\xi_e\omega_e\dot{Q} + \omega_e^2 Q + \frac{\theta_i}{LC_{pi}} q_i + \frac{V_{nl}}{L} = 0. \tag{2b}$$

In the above equations, $Q(t)$ is the electric charge in one of the electrodes of the PE patch and (m_i, ξ_i, $\hat{\omega}_i$, F_i, θ_i) are

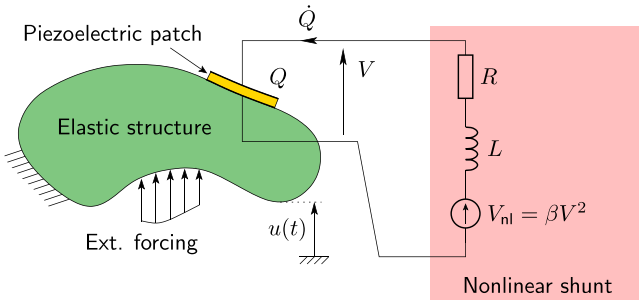

Figure 1. Nonlinear shunt principle.

respectively the modal mass, damping, natural frequency in open circuit ($Q = 0$), forcing and piezoelectric coupling coefficient of the ith mode. $C_{\text{p}i}$ is the effective capacitance of the piezoelectric patch [7], and the electrical natural frequency and damping factor are defined by:

$$\omega_{\text{e}} = \frac{1}{\sqrt{LC_{\text{p}i}}}, \quad \xi_e = \frac{R}{2}\sqrt{\frac{C_{\text{p}i}}{L}}, \tag{3}$$

where (R,L) are respectively the resistance and the inductance of the electric circuit. $V_{\text{nl}}(t)$ represents the nonlinear voltage source added to the shunt circuit, that is chosen to include quadratic nonlinearities to activate the 2:1 internal resonance. In this study, $V_{\text{nl}}(t)$ is taken to be proportional to the square of the voltage $V(t)$ across the piezoelectric patch, by a constant gain β, as shown in figure 1. Another choice could be a nonlinear voltage proportional to the square of the electric charge in the PE patch electrode (i.e. $V_{\text{nl}} = \beta Q^2$). As shown in [1], this latter choice would lead to a huge value of β (of the order of 10^{15} V/C^2) to achieve the absorber's design conditions, unrealistic in practice. One has thus:

$$V_{\text{nl}} = \beta V^2, \quad V = \frac{1}{C_{\text{p}i}}\left(Q + \theta_i q_i\right), \tag{4}$$

where the second equation is the classical constitutive law of the PE patch [1]. We also define the dimensionless electromechanical modal coupling factor (EMMCF) of the ith mode as [29]:

$$k_i^2 = \frac{\hat{\omega}_i^2 - \check{\omega}_i^2}{\hat{\omega}_i^2} = \frac{\theta_i^2}{\hat{\omega}_i^2 C_{\text{p}i} m_i}, \tag{5}$$

with $\check{\omega}_i$ the natural frequency in short circuit ($V = 0$).

To simplify the writing of the governing equations (2*a*) and (2*b*), we define the following parameters:

$$\tau = \hat{\omega}_i t, \quad \bar{q}_i = \sqrt{m_i} q_i, \quad \bar{Q} = \sqrt{L} Q, \quad r_i = \frac{\omega_e}{\hat{\omega}_i}, \% \quad \delta_i = k_i r_i, \tag{6a}$$

$$\bar{F}_i = \frac{F_i}{\hat{\omega}_i^2 \sqrt{m_i}} \quad \bar{V}_{\text{nl}} = \frac{V_{\text{nl}}}{\hat{\omega}_i^2 \sqrt{L}} \quad \bar{\Omega} = \frac{\Omega}{\hat{\omega}_i} \tag{6b}$$

to obtain a system in term of $\hat{q}_i$ and $\hat{Q}$ with symmetric coupling terms:

$$\ddot{\bar{q}}_i + 2\xi_i \dot{\bar{q}}_i + \bar{q}_i + k_i r_i \bar{Q} = \bar{F}_i \cos\bar{\Omega}\tau, \tag{7a}$$

$$\ddot{\bar{Q}} + 2\xi_e r_i \dot{\bar{Q}} + r_i^2 \bar{Q} + k_i r_i \bar{q}_i + \bar{V}_{\text{nl}} = 0, \tag{7b}$$

where the derivatives in equation (7) are with respect to the dimensionless time τ. Note that the unknowns $(\bar{q}_i, \bar{Q})$ share the same unit (m kg$^{1/2}$). Moreover, an important parameter is r_i, the ratio between the electrical natural frequency (linked to the resonant electric circuit) and the mechanical natural frequency, that will be chosen close to 0.5 to achieve the 2 : 1 internal resonance.

Since equations (2*a*), (2*b*) or (7*a*), (7*b*) are linearly coupled because of the piezoelectric coupling, this latter system is diagonalized by further expanding the unknowns $(\bar{q}_i, \bar{Q})$ on the electromechanical modal basis, constituted of two modes $\boldsymbol{\Psi}_k$, $k = 1, 2$ such that:

$$\boldsymbol{\Psi}_1 = \begin{pmatrix} -\varepsilon \\ 1 \end{pmatrix}, \quad \boldsymbol{\Psi}_2 = \begin{pmatrix} 1 \\ \varepsilon \end{pmatrix}, \tag{8}$$

with

$$\varepsilon = \frac{2k_i r_i}{1 - r_i^2 + \sqrt{\Delta}}, \tag{9}$$

and the associated eigenfrequencies:

$$\omega_1^2 = \frac{1 + r_i^2 - \sqrt{\Delta}}{2}, \quad \omega_2^2 = \frac{1 + r_i^2 + \sqrt{\Delta}}{2}, \tag{10}$$

with $\Delta = (1 - r_i^2)^2 + 4k_i^2 r_i^2$. The modal expansion reads:

$$\begin{pmatrix} \bar{q}_i(\tau) \\ \bar{Q}(\tau) \end{pmatrix} = \sum_{k=1}^{2} \boldsymbol{\Psi}_k x_k(\tau) = \begin{pmatrix} -\varepsilon x_1(\tau) + x_2(\tau) \\ x_1(\tau) + \varepsilon x_2(\tau) \end{pmatrix}. \tag{11}$$

Because the electromechanical coupling is often small ($k_i < 0.2$), ε is also small (of the same order of magnitude) and the two electromechanical modes are very close to a purely electrical mode for $\boldsymbol{\Psi}_1$ ($x_1 \simeq \bar{Q}$) and a purely mechanical mode for $\boldsymbol{\Psi}_2$ ($x_2 \simeq \bar{q}_i$). The same rule applies to the eigenfrequencies ω_1 and ω_2, which are close to the dimensionless uncoupled natural frequencies $\omega_e/\hat{\omega}_i = r_i$ and $\hat{\omega}_i/\hat{\omega}_i = 1$. Precisely, because of the small positive term $4k_i^2 r_i^2$ in Δ, (ω_1, ω_2) are slightly out of the frequency band $[r_i, 1]$ ($\omega_1 \lesssim r_i$; $\omega_2 \gtrsim 1$). Consequently, the mechanical resonance of the system appears at a dimensioned frequency $\tilde{\omega}_i = \omega_2 \hat{\omega}_i$, which is slightly above the open circuit frequency $\hat{\omega}_i$. Moreover, the tuning of the electrical mode at almost half the frequency of the mechanical mode to achieve the 2:1 internal resonance, must be prescribed on the electromechanical natural frequency ratio ω_1/ω_2, which is slightly lower than $r_i = \omega_e/\hat{\omega}_i$. This is quantitatively illustrated in figure 2, which shows that for a targeted value of ω_1/ω_2, r_i must be chosen slightly larger (for instance, $r_i = 0.543$ for $\omega_1/\omega_2 = 0.5$ and $k_i = 0.2$).

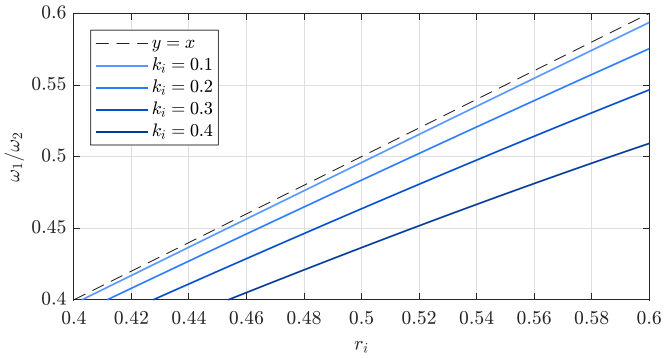

Figure 2. Electromechanical natural frequency ratio ω_1/ω_2 (from equations (10)) as a function of the frequency ratio r_i, for various values of the EMMCF k_i, as specified.

After modal expansion and using the definition (4) of V_{nl}, one obtains [1]:

$$\ddot{x}_1 + 2\mu_1\dot{x}_1 + \omega_1^2 x_1 + \Lambda_1 x_1^2 + \Lambda_2 x_1 x_2 + \Lambda_3 x_2^2 = f_1 \cos\bar{\Omega}\tau, \tag{12a}$$

$$\ddot{x}_2 + 2\mu_2\dot{x}_2 + \omega_2^2 x_2 + \Lambda_4 x_1^2 + \Lambda_5 x_1 x_2 + \Lambda_6 x_2^2 = f_2 \cos\bar{\Omega}\tau. \tag{12b}$$

In the above system, we assume that the modal mass is such that $1+\varepsilon^2 \approx 1$ since $\varepsilon \ll 1$ and that the non-diagonal damping terms are neglected since they are small and have thus a negligible effect on the dynamics [30]. The expressions of the damping terms μ_1 and μ_2, the nonlinear coefficients Λ_k, and the modal forcing terms f_1 and f_2 are given in [1]. This last system (12*a*) and (12*b*) is at the basis of the theoretical analysis of [1] since it is the canonical system to study the 2:1 internal resonance and its dynamical effects (nonlinear antiresonance and saturation phenomenon), as recalled in the following.

2.2. Typical response and saturation phenomenon

To illustrate the main features of the 2:1 internal resonance used for our absorber design, a first order solution of system (12*a*) and (12*b*), in the case of the 2:1 internal resonance ($\omega_2 \approx 2\omega_1$), can be written [1, 31]:

$$x_1(\tau) = a_1 \cos\left(\frac{\bar{\Omega}}{2}\tau - \frac{\gamma_1+\gamma_2}{2}\right), x_2(\tau) = a_2 \cos\left(\bar{\Omega}\tau - \gamma_2\right), \tag{13}$$

where a_1 and a_2 are the amplitudes, γ_2 is the phase angle of $x_2(\tau)$, and γ_1 represents the relative phase angle between $x_1(\tau)$ and $x_2(\tau)$. The closed-form expressions of the amplitudes and phase angles (obtained with a first order multiple scale, MSM), in addition to a detailed theoretical study, can be found in [1]. A typical example is illustrated in figure 3. It shows the response of amplitudes a_1 and a_2 with respect to the detuning $\sigma_1 = \bar{\Omega} - \omega_2$ for different excitation levels. Two main features are visible:

- there exists a threshold force for the excitation f_2 above which the linear response enters an instability region (shaded in blue). In this region, the energy transfer from the high to low-frequency modes occurs, and the linear response loses its stability. This activates the response of a_1, which increases with the excitation, while a_2 tends to have a *kind of antiresonance* in place of the linear resonance frequency (see figure 3(a));
- focusing on the amplitudes at the resonance frequency (a_1^* and a_2^*), it can be observed in figure 3(b) that a_2^* becomes independent of the excitation level, a feature called a *saturation phenomenon*, whereas a_1^* keeps increasing. Note that the same analysis could be drawn at any other frequency that lies in the frequency range of the instability region since the a_2 curve is independent of f_2.

Another major feature of this system is related to phase γ_1. The analytical results suggest that γ_1 is monotonic as a function of the excitation frequency Ω, independent of the excitation level f_2, and *always locked at a value of* $3\pi/2\,[2\pi]$ at the antiresonance frequency ($[2\pi]$ means modulo 2π).

2.3. Response in the physical space

Figure 3 and equations (12*a*) and (12*b*) are related to the electromechanical coordinates $x_1(\tau)$ and $x_2(\tau)$. To go back to the physical coordinates (the mechanical displacement and the electric charge), the modal transform of equation (11) is used to write:

$$\boldsymbol{u}(t) = \frac{\boldsymbol{\Phi}_i}{\sqrt{m_i}}\left[\underbrace{-\varepsilon a_1 \cos\left(\frac{\Omega}{2}t - \frac{\gamma_1+\gamma_2}{2}\right)}_{x_1(t)} + \underbrace{a_2\cos\left(\Omega t - \gamma_2\right)}_{x_2(t)}\right], \tag{14a}$$

$$Q(t) = \frac{1}{\sqrt{L}}\left[\underbrace{a_1 \cos\left(\frac{\Omega}{2}t - \frac{\gamma_1+\gamma_2}{2}\right)}_{x_1(t)} + \underbrace{\varepsilon a_2\cos\left(\Omega t - \gamma_2\right)}_{x_2(t)}\right]. \tag{14b}$$

Consequently, $\boldsymbol{u}(t)$ and $Q(t)$ are mainly composed of two harmonics, at $\Omega/2$ (harmonic H1/2) and at Ω (harmonic H1). Because of the small value of ε, the leading harmonics in the response of $\boldsymbol{u}(t)$ and $Q(t)$ are, respectively, H1 and H1/2, so that, at the antiresonance, the energy is transferred from the mechanical mode to the electrical mode and from the frequency Ω to its subharmonic $\Omega/2$.

2.4. Effect of nonresonant terms

The first order analytical solution that leads to figure 3 (using the multiple scale method, MSM) naturally neglects the nonresonant nonlinear terms of system (12*a*) and (12*b*), namely the terms of coefficients Λ_1, Λ_3, Λ_5, Λ_6. Indeed, the skeleton of the dynamics under 1:2 internal resonance is constituted by the resonant terms (of coefs. Λ_2 and Λ_4) which are responsible

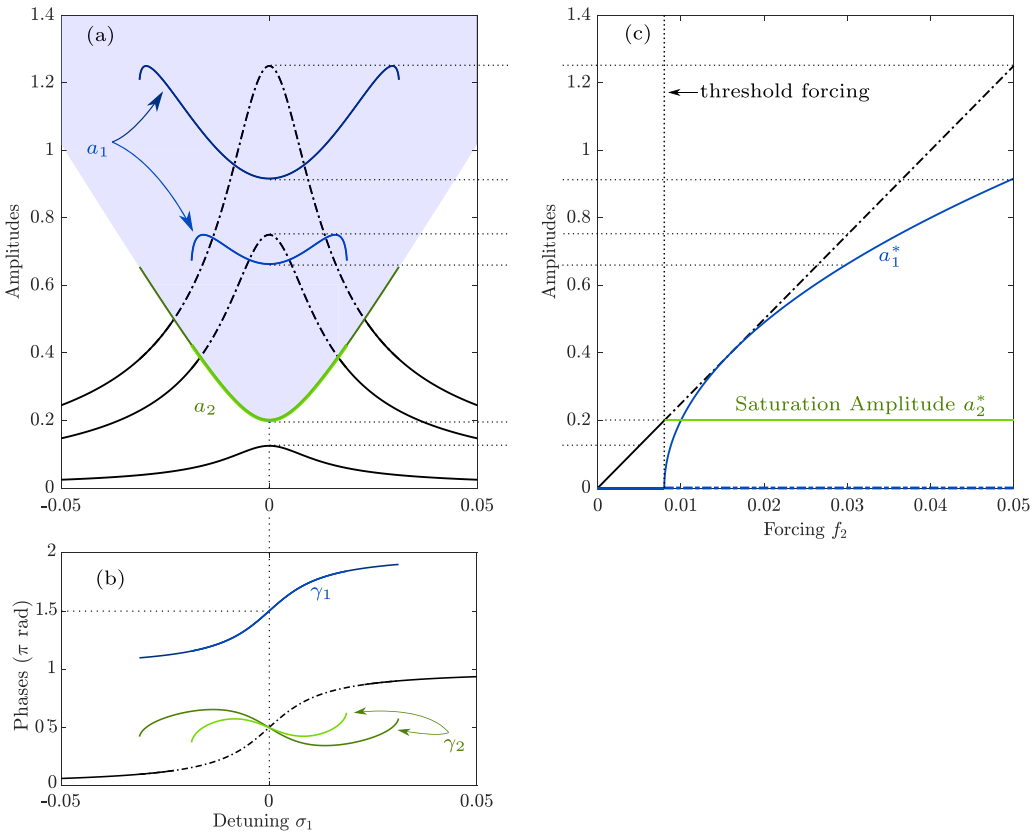

Figure 3. Typical response of the amplitudes a_1 and a_2 and the phases γ_1 and γ_2, stemming from the first order multiple scale solution of system (12*a*) and (12*b*), for $\omega_2 = 2\,\omega_1$ and by neglecting the nonresonant terms, from [1]. The numerical values are $\Lambda_2 = \Lambda_4 = 0.1$, $\mu_1 = 0.005$, $\mu_1 = 0.01$. (a) and (b) show respectively the amplitude and phase response with respect to the detuning σ_1 for values of the forcing f_2 ($f_2 \in \{0.005; 0.03; 0.05\}$). (c) amplitude response at the resonance frequency ($\sigma_1 = 0$) with respect to the excitation level f_2. In the plots, the linear responses of a_2 and γ_2 are plotted in black. The solid and the dashed-dotted lines denote respectively the stable and the unstable solutions.

for the strong coupling between the modes (see [1, 31, 32] for the analytical solution and [33, 34] for details about resonant terms). However, it is shown in [1] that in the present case of a nonlinear shunt, the order of magnitude of Λ_1 is larger than the one of Λ_2 and Λ_4, leading to an unusual and major effect of the corresponding non-resonant term, which quantitatively modifies the ideal response of figure 3.

This is illustrated in figure 4 in which a numerical solution of equations (2*a*) and (2*b*) (obtained with the continuation software Manlab [35, 36]) is shown. To be more precise, we considered the case of the first bending mode of the cantilever beam structure shown in figure 6, with the displacement $u(t)$ considered at the beam tip ($u(t) = q_i(t)$ with a mode shape scaled to 1). The modal parameters used in the numerical simulations are the ones found experimentally and gathered in table.

By observing the physical response of the amplitudes corresponding to the H1 and H1/2 harmonics of the displacement and charge (u_{H1} and $Q_{H/12}$), shown in figure 4, and by comparison with the typical response illustrated in figure 3, the effect of the non-resonant terms can be inferred [1]:

- the antiresonance shifts to the low frequencies with increasing excitation level, violating the saturation phenomenon;
- although the antiresonance is shifting, its amplitude remains constant at a saturation amplitude u_{H1}^*, which is the same as a_2^* analytically obtained with the MSM;
- the phase angle γ_1 is kept locked at $3\pi/2$ at the antiresonance point;
- a break in the response symmetry is observed, leading to another peak to the right of the resonance peak and the appearance of a softening behavior, as it can be seen in the charge response.

The main aim of this work is to exploit the saturation phenomenon, which is broken because of the non-resonant terms intrinsically related to the nonlinear shunt. To correct this, we proposed an antiresonance correction (AR correction) technique, that consists in locking the antiresonance by choosing the proper value of the ratio r_i for each excitation level *to counter-balance* the shifting observed in figure 4. As shown in detail in [1], this can be simulated by a numerical continuation of the system (2*a*) and (2*b*) using Manlab, to obtain the amplitude of u_{H1} as a function of r_i for a certain excitation level and with a prescribed driving frequency equal to the resonance frequency shown in figure 4 ($\tilde{\omega}_1 = 37.7$ Hz). Then, the value of r_i where u_{H1} achieves its minimum value is the required value to lock the antiresonance at the resonance frequency.

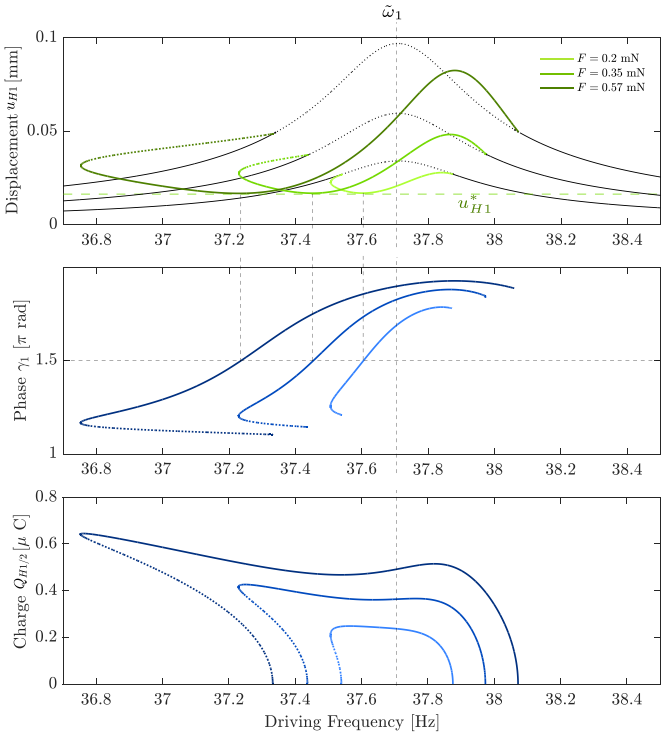

Figure 4. Frequency response of the beam tip displacement first harmonic u_{H1} amplitude, the charge $Q_{\mathrm{H1}/2}$ subharmonic and the phase γ_1, obtained by solving system (2*a*) and (2*b*) using Manlab for several excitation levels. The numerical values are $\beta = 0.012$, $r_i = 0.52$, $\xi_e = 0.002$, and the mechanical damping coefficient is $\xi_1 = 0.005$. The displacement linear response is plotted in black. The solid and dotted lines denote, respectively, the stable and the unstable solutions.

Following the AR correction, the response of u_{H1} shown in figure 4 is replaced by the one shown in figure 5(a) where it clearly shows that the antiresonance is locked at $\tilde{\omega}_1$. One can note the appearance of a quasi-periodic solution (QP) for $F = 0.57$ mN. Also, figure 5(b) shows the amplitude of u^*_{H1} with respect to the excitation level where one can observe that the proposed AR correction preserves the saturation phenomenon.

Experimentally, the AR correction will be performed analogously, using the preserved feature of $\gamma_1 = 3\pi/2$ at the antiresonance point. Namely, for a certain excitation level and by prescribing the driving frequency at $\tilde{\omega}_i$, the required value of r_i, which is controlled by the inductance in the circuit, is the one that locks γ_1 at $3\,\pi/2$. This will be illustrated in detail in section 4.4.

2.5. Summary on the theoretical results

The main conclusions that can be drawn from the above theoretical analysis in addition to the analysis done in detail in our theoretical paper [1] are as follows:

- Connecting the proposed nonlinear shunt circuit to an arbitrary structure via a PE patch leads to an electromechanical system governed by a fully quadratic nonlinear system (12*a*) and (12*b*). By tuning $\hat{\omega}_i \approx 2\omega_e$, a 2:1 internal resonance occurs, leading to an energy transfer from the mechanical mode to be attenuated to the electrical mode designated by the shunt circuit.
- The saturation phenomenon is violated as seen in figure 4. To preserve this phenomenon, we propose an antiresonance correction by slightly tuning the value of r_i for each excitation level, by locking the phase γ_1 at $3\pi/2$.

3. Experimental details

3.1. Structure under test

The experimental tests were conducted on a cantilever beam with two PIC 151 piezoelectric (PE) patches symmetrically glued on the two faces of a stainless steel beam, as shown in figure 6. The nonlinear shunt circuit is connected to the structure with the PE patches in series and with opposite polarizations to couple the electric shunt circuit to the bending of the beam [37]. A contactless electromagnetic actuator composed of a fixed coil and a magnet attached to the structure tip is used to generate an electromagnetic force by inducing a current in the coil. In [38], a detailed design has been illustrated for such a coil-magnet system and a linear relationship has been found between the current $I(t)$ induced in the coil and the resulting forcing $F(t)$:

$$F(t) = \alpha I(t), \tag{15}$$

where α is a constant.

3.2. Experimental modal analysis

Before conducting the experiments with the nonlinear shunt circuit, an experimental modal analysis was performed to identify the parameters of our model of the electromechanical system under test. The experimental modal analysis shown here consists of utilizing the benefit of the piezoelectric coupling between the mechanical and electrical domains (i.e. the structure and the shunt circuit). Focusing on a particular mechanical mode of the structure (the ith), we normalize its mode shape with its value at the tip x_t of the beam, such that $\phi_i(x_t) = 1$. Considering the transverse displacement $u(t)$ of the beam at its tip and a colocalized point forcing $F(t) = F_0 \cos \Omega t$ (see figure 6), equation (1) shows that $u(t) \equiv q_i(t)$ and $F_i = F_0$ in equation (2*a*). We then consider two sets of experiments:

- a mechanical forcing with the PE patches either in short ($V = 0$) or open ($Q = 0$) circuit, leading to the two frequency response functions (FRFs) (from equations (2*a*), (2*b*) and (4)):

$$H_1(\Omega) = \left.\frac{\mathring{u}}{\mathring{I}}\right|_{V=0} = \frac{\gamma_i}{\Omega^2 - \tilde{\omega}_i^2 + 2j\xi_i\hat{\omega}_i\Omega},$$
$$\hat{H}_1(\Omega) = \left.\frac{\mathring{u}}{\mathring{I}}\right|_{Q=0} = \frac{\gamma_i}{\Omega^2 - \hat{\omega}_i^2 + 2j\xi_i\hat{\omega}_i\Omega}. \tag{16}$$

Notice that the difference between H_1 and $\hat{H}_1$ is the short/open natural circuit frequencies $\tilde{\omega}_i$ or $\hat{\omega}_i$.

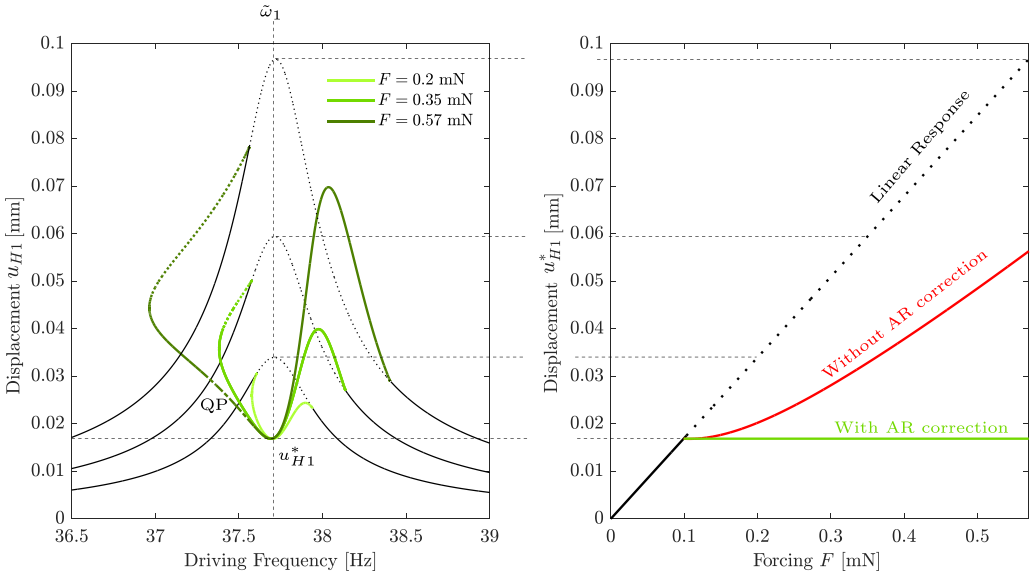

Figure 5. (a) Frequency response of the first harmonic amplitude of the beam tip displacement u_{H1}, estimated by solving system (2*a*) and (2*b*) using Manlab, for several excitation levels and with AR correction. (b) First harmonic amplitude of the beam tip displacement at the resonance frequency u^*_{H1} with respect to the excitation level, with and without AR correction. The numerical values are $\beta = 0.012$ and $\xi_1 = 0.005$. The displacement linear response is plotted in black. The solid and dotted/dashed lines denote, respectively, the stable and unstable solutions. QP refers to a quasi-periodic response, obtained after a loss of stability due to Neimark-Sacker bifurcations.

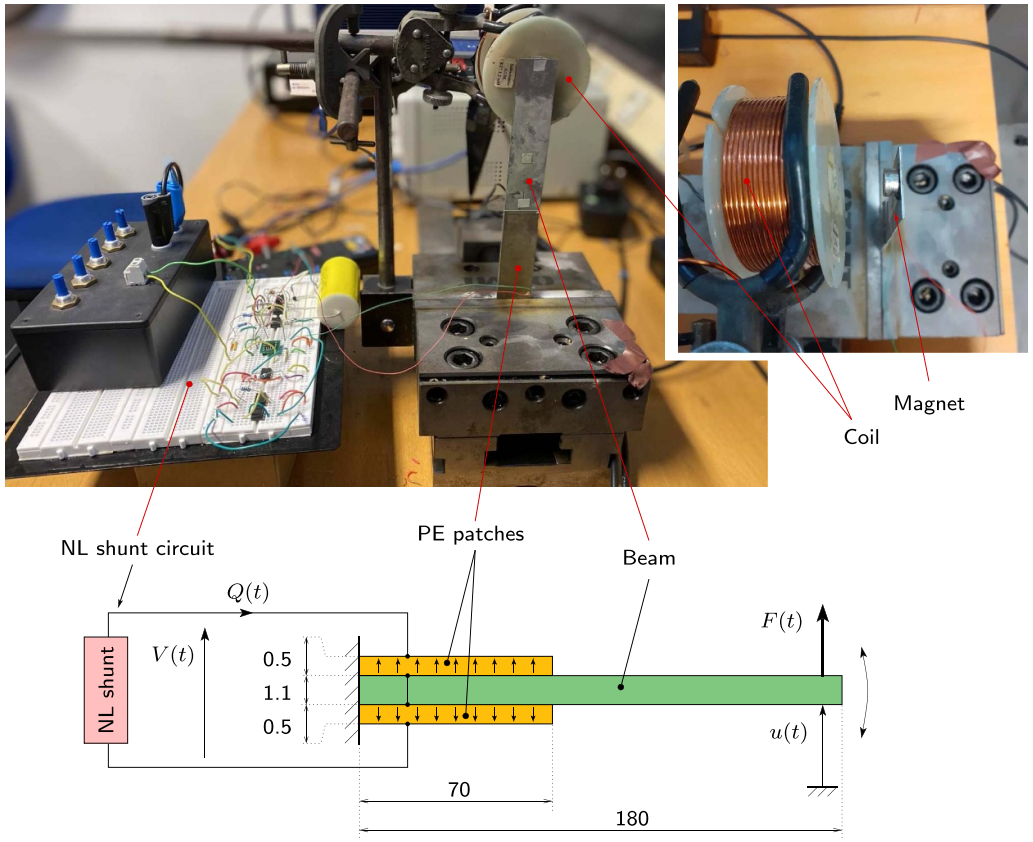

Figure 6. Experimental setup. Dimensions are in mm. The width of the beam and PE patches is 30.5 mm.

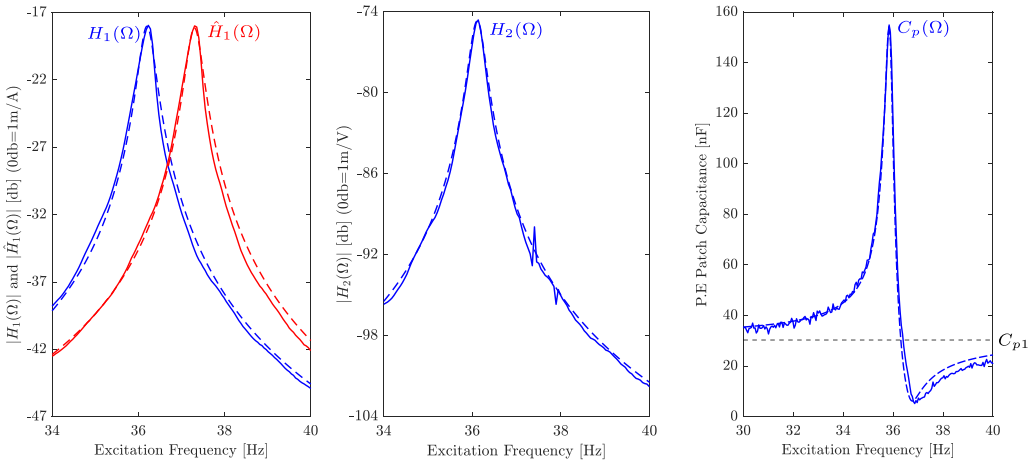

Figure 7. Fitting between experimental and analytical FRFs. The solid and dashed lines depict the experimental and the analytical results, respectively.

Table 1. Electro-mechanical modal parameters of the first bending mode of the cantilever beam (subscript $i = 1$).

Parameters	$\omega_1/(2\pi)$ (Hz)	$\hat{\omega}_1/(2\pi)$ (Hz)	$\xi_1(\%)$	k_1	θ_1(mN V^{-1})	$m_1[g]$	α (N/A)	C_{p1} (nF)
Value	36.6	37.51	0.5	0.20	0.8	8.8	0.6	32.45

- an electrical forcing by prescribing the voltage $V(t)$ without mechanical forcing, that conducts to define:

$$H_2(\Omega) = \left.\frac{\mathring{u}}{\mathring{V}}\right|_{F=0} = -\frac{\lambda_i}{\Omega^2 - \breve{\omega}_i^2 + 2j\xi_i\hat{\omega}_i\Omega},$$
$$C(\Omega) = \left.\frac{\mathring{Q}}{\mathring{V}}\right|_{F=0} = C_{pi} + \frac{\delta_i}{\Omega^2 - \breve{\omega}_i^2 + 2j\xi_i\hat{\omega}_i\Omega}. \qquad (17)$$

In the above equations, $\mathring{\bullet}(\Omega)$ is the Fourier transform of $\bullet(t)$ and the amplitude constants reads:

$$\gamma_i = \frac{\alpha}{m_i}, \quad \lambda_i = \frac{\theta_i}{m_i}, \quad \delta_i = \frac{\theta_i^2}{m_i}. \qquad (18)$$

By fitting the FRFs of equations (16) and (17) on the experiments, it is possible to estimate the values of the unknown parameters of the ith mode of the structure: $\breve{\omega}_i$, $\hat{\omega}_i$, ξ_i, m_i, θ_i, C_{pi} and α, as well as the EMMCF k_i with equation (5). Notice that in the first sets of experiments, one could also measure the FRF $\mathring{Q}/\mathring{F}$ (with $\mathring{F} = \alpha\mathring{I}$), which is theoretically equal to H_2 in the second step of experiments (following equations (2*a*) and (2*b*), which is also a consequence of the Maxwell-Betti reciprocity theorem). This could give another set of measurements to improve the parameter estimation because of the redundancy. However, it was not possible to measure Q and I at the same time, since we had only one available current probe in the laboratory.

In practice, we estimated the parameters of the first mode of the experimental beam. We measured the FRFs with a chirp signal as input. For the mechanical forcing, a Brüel & Kjær 2719 power amplifier connected to the coil was used; for the electrical forcing, we used a TREK PZD700A piezoelectric amplifier. In both cases, a Polytec OFV-505 vibrometer measured the velocity at the tip of the beam, and a PHILIPS PM 9355 precision current clamped was used to measure the current intensity, either in the coil ($I(t)$) for the first set of experiments, or in the piezoelectric circuit to obtain the charge $Q(t)$, for the second sets of experiments. The piezoelectric voltage was obtained with the voltage monitor of the TREK amplifier. A M+P international analyzer was used to generate the input signal and compute the FRFs.

Figure 7 shows the experimental FRFs and the obtained fitting, that directly give the open and short circuit frequencies (ω_1 and $\hat{\omega}_1$), the damping coefficient ξ_1 and the effective capacitance C_{p1}. The gains γ_1, λ_1, and δ_1 are also determined directly and used to estimate the other modal parameters: the modal mass m_1, the coupling coefficient θ_1 and the mechanical forcing constant α as follows: $\theta_1 = \delta_1/\lambda_1 \Rightarrow m_1 = \theta_1/\lambda_1 \Rightarrow \alpha = \gamma_1\, m_1$. Finally, the EMMCF is obtained using the second equation (5) ($k_1 = \theta_1/\hat{\omega}_1/\sqrt{m_1 C_{p1}}$). The deduced modal parameters numerical values are gathered in table 1. Notice that the value of k_1 estimated with the open/short circuit frequencies (the first equation (5)) is slightly larger: $k_1 = 0.22$. The value $k_1 = 0.2$ was however kept since it leads to an excellent match between theory and experiments, seen in figure 7. Moreover, in the process, the velocity and current signals are divided by $j\Omega$ to get the displacement and charge.

3.3. Nonlinear shunt circuit description

The nonlinear shunt circuit used in the tests is shown in figure 8. It consists of three sub-circuits to realize (a) a tunable synthetic inductor (outlined in blue in the figure 8). (b) a voltage measurement (orange). (c) a nonlinear voltage generator (light red). Preliminary simulations of the circuit showed that fairly large voltages appear, especially during transients. Hence, the operational amplifiers OA_1 to OA_6 are OPA445 (Texas Instruments) which can operate up to ± 40 V input

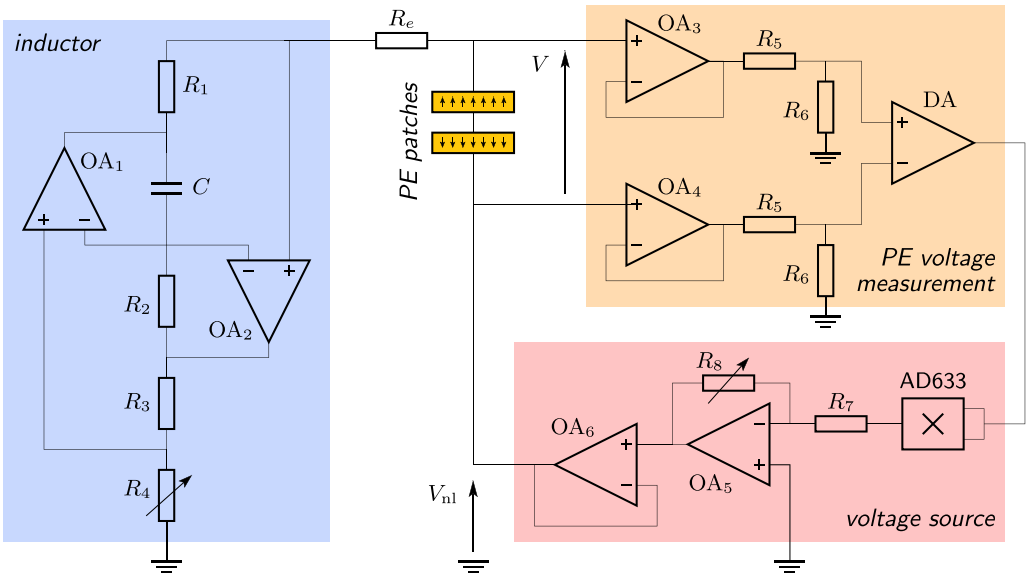

Figure 8. Nonlinear shunt circuit design.

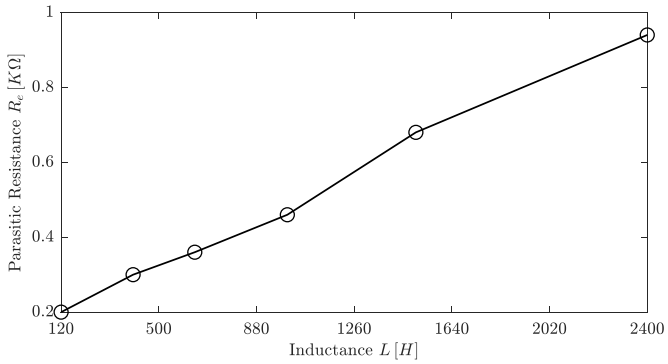

Figure 9. Experimental estimation of the parasitic resistance R_e as function of the inductance L.

and output voltage and supply 15 mA to drive the patches. To obtain an electrical resonance frequency close to half the mechanical resonance frequency, an inductance *ca* 2000 H is required for the beam. Therefore, a synthetic inductor is realized using an Antoniou circuit [11, 39], which can achieve large inductor values, given by

$$L = \frac{R_1\, R_2\, R_4\, C}{R_3}. \tag{19}$$

The L value is tuned using the variable resistor R_4. According to the theory, the nonlinear shunt is more effective if the electric damping is null, since it leads to a perfect antiresonance (a zero mechanical mode amplitude, see [1]). In practice, however, it was noticed that this circuit introduces a parasitic resistance as already observed in [40]. The resistance R_e in series with the Antoniou synthetic inductor accounts for this problem in the schematic. The dependence of R_e on L was estimated by testing the Antoniou inductor circuit in series with a 33 nF capacitor to realize a resonant circuit then fit the FRF response. This relationship is shown in figure 9, which was later used during the experiment to assess the results.

Table 2. Fixed component values in the nonlinear shunt circuit.

Component	R_1(kΩ)	R_2(kΩ)	R_3(kΩ)	C(μF)	R_5(kΩ)	R_6(kΩ)	R_7(kΩ)
Value	2	1	1	10	82	22	3.8

The voltage measurement is ensured by two voltage dividers involving the resistor R_5 and R_6, which are decoupled using two voltage followers (OA$_3$ and OA$_4$) in order to avoid further introduction of parasitic resistance. The voltage across the patches is thus measured and attenuated to a level compatible with the differential amplifier DA (INA826, Texas Instrument), which ensures noise rejection. Finally, the quadratic non-linearity is realized using a multiplier (AD633, Analog Device) amplified by an inverting amplifier (OA$_5$) with a tunable gain thanks to R_8 to control β (cf equation (4)) as follows

$$\beta = \frac{R_8}{10\, R_7}\left(\frac{R_6}{R_5 + R_6}\right)^2. \tag{20}$$

The resulting voltage V_{nl} is then supplied to the patches by the follower (OA$_6$) to ensure a low output impedance. Table 2 gathers the actual values of the components used throughout the experiments presented.

3.4. Nonlinear frequency responses measurements

3.4.1. Measurement of leading harmonics. As discussed in section 2.3, when considering the 2:1 internal resonance, an energy transfer is expected to occur from the driven mechanical mode to an electrical mode at half the driven frequency. To experimentally validate the energy transfer and the nonlinear shunt behavior exhibited by the theoretical results of section 2,

we are only interested in the amplitudes and phase angles of the fundamental harmonic (H1) of the structure tip displacement $u(t)$ and the subharmonic (H1/2) of the charge $Q(t)$ in the PE patch electrodes. Following equation (14), we denote them by:

$$u(t) = u_{\mathrm{H1}} \cos(\Omega t - \gamma_2) + \mathrm{oh},$$
$$Q(t) = Q_{\mathrm{H1}/2} \cos\left(\frac{\Omega}{2} t - \frac{\gamma_1 + \gamma_2}{2}\right) + \mathrm{oh}, \qquad (21)$$

with 'oh' meaning 'other harmonics' and u_{H1}, $Q_{\mathrm{H1}/2}$ denoting their amplitudes. In practice, we estimate $u(t)$ and $Q(t)$ by measuring the velocity $v(t)$ of the structure tip with a laser vibrometer (Polytec 0FV 505) and the voltage across the PE patches terminals $V(t)$ with a differential voltage probe (Française d'Instrumentation ST 500-5). Those two signals can be written:

$$v(t) = v_{\mathrm{H1}} \cos(\Omega t - \varphi_v) + \mathrm{oh},$$
$$V(t) = V_{\mathrm{H1}/2} \cos(\Omega/2\, t - \varphi_V) + \mathrm{oh} \qquad (22)$$

with $(v_{\mathrm{H1}}, \varphi_v)$, $(V_{\mathrm{H1}/2}, \varphi_V)$ denoting their amplitude/phase pairs. Taking the time derivative of $u(t)$ in equation (21) leads to:

$$v_{\mathrm{H1}} = \Omega\, u_{\mathrm{H1}}, \quad \varphi_v = \gamma_2 - \pi/2. \qquad (23)$$

To find the relation between $V(t)$ and $Q(t)$, we rewrite equation (4) as:

$$V(t) = \frac{1}{C_{\mathrm{pi}}} \Big[Q(t) + \theta_1 u(t) \Big], \qquad (24)$$

since $\phi_i(x_t) = 1$ as explained in section 3.2. Then, replacing in equation (24) the H1/2 harmonics of $u(t)$ and $Q(t)$ of equations (14*a*) and (14*b*) and eliminating a_1, one obtains:

$$V_{\mathrm{H1}/2} = \frac{Q_{\mathrm{H1}/2}}{C_{\mathrm{pi}}} \left(1 - \frac{\varepsilon \theta_i \sqrt{L}}{\sqrt{m_i}}\right), \quad \varphi_V = (\gamma_1 + \gamma_2)/2. \qquad (25)$$

The order of magnitude of the second term in the above expression of $V_{\mathrm{H1}/2}$, directly related to the electromechanical coupling, can be evaluated by using the following relations: $\varepsilon \simeq k_i r_i/(1 - r_i^2)$ (obtained by neglecting $4k_i^2 r_i^2$ in Δ in equation (9), see [1]), $\theta_i = k_i \hat{\omega}_i \sqrt{C_{\mathrm{pi}} m_i}$ (equation (5)) and $\sqrt{L} = 1/(\omega_e \sqrt{C_{\mathrm{pi}}})$. After simplifications, one obtains:

$$\frac{\varepsilon \theta_i \sqrt{L}}{\sqrt{m_i}} \simeq \frac{k_i^2}{1 - r_i^2} \simeq \frac{4k_i^2}{3} < 8.3 \cdot 10^{-2}, \qquad (26)$$

for a tuned nonlinear shunt with $r_i \simeq 1/2$ and $k_i < 0.25$. Consequently, even for a high piezoelectric coupling of $k_i = 25\%$, the above term is more than one order of magnitude smaller than one, and can be neglected, leading to:

$$V_{\mathrm{H1}/2} \simeq Q_{\mathrm{H1}/2}/C_{\mathrm{pi}}. \qquad (27)$$

In conclusion, the amplitude and phase of the leading harmonics of the beam tip displacement and the electric charge are directly estimated by the H1 harmonics of the velocity and the H1/2 harmonics of the PE voltage, using equations (23), (25) and (27).

3.4.2. Harmonics amplitude and phase estimation using demodulation. Since the response of the system is highly nonlinear due to the nonlinear shunt, to validate the theory of figure 4, we prescribe a harmonic force $F(t) = F_0 \cos \Omega t$ at the beam's tip, with the coil/magnet device described in section 3.1, and we perform stepped sine experiments. It consists in choosing a given discrete set of values of Ω around the resonance frequency $\tilde{\omega}_1$ of the structure's first bending mode. For each frequency, the excitation frequency and level (measured by a current clamp) are kept constant until the steady-state is reached, in which several periods of the beam tip velocity $v(t)$ and the PE voltage $V(t)$ are recorded, before stepping to the next discrete frequency. The same measuring devices than in section 3.2 (B&K 2719, PM 9355, OFV 505 & ST 500-5) were used. The input/output signals were synthesized/measured with National Instrument cards (NI-9234, NI-9263) driven by a Matlab program.

At each excitation frequency, the harmonics amplitude and the phase angles are extracted by a demodulation procedure [41] (also known as synchronous or homodyne detection). Each measured signal $s(t)$ is multiplied by sine/cosine signals at the frequency of the leading harmonic, and the result is averaged over a number of periods. Namely, if $s(t)$ is periodic:

$$s(t) = s_0 + \sum_{h=1}^{+\infty} s_h \cos(h\Omega t - \varphi_h), \qquad (28)$$

one obtains for the kth harmonic:

$$I_{\mathrm{c}} = \langle s(t) \cos k\Omega t \rangle_{n_k T_k} = \frac{s_k}{2} \cos \varphi_k,$$
$$I_{\mathrm{s}} = \langle s(t) \sin k\Omega t \rangle_{n_k T_k} = \frac{s_k}{2} \sin \varphi_k, \qquad (29)$$

where

$$\langle \bullet(t) \rangle_{n_k T_k} = \frac{1}{n_k T_k} \int_0^{n_k T_k} \bullet(t) \mathrm{d}t \qquad (30)$$

is the average of the signal $\bullet(t)$ over a duration equal to n_k harmonic periods $T_k = 2\pi/(k\Omega)$. Consequently, the kth harmonic amplitude and phase are obtained by:

$$s_k = 2\sqrt{I_{\mathrm{c}}^2 + I_{\mathrm{s}}^2}, \quad \varphi_k = \arg(I_{\mathrm{c}} + jI_{\mathrm{s}}). \qquad (31)$$

In our case, we used $k = 1$ to estimate the H1 harmonic of $v(t)$ and $k = 1/2$ for the H1/2 harmonic of $V(t)$. In practice, the integral in equation (30) was performed with a trapezoidal numerical integration and the number n_1 of periods used in the averages of equation (29) to estimate the H1 harmonics of $v(t)$ was chosen even to exactly filter the subharmonic part of the

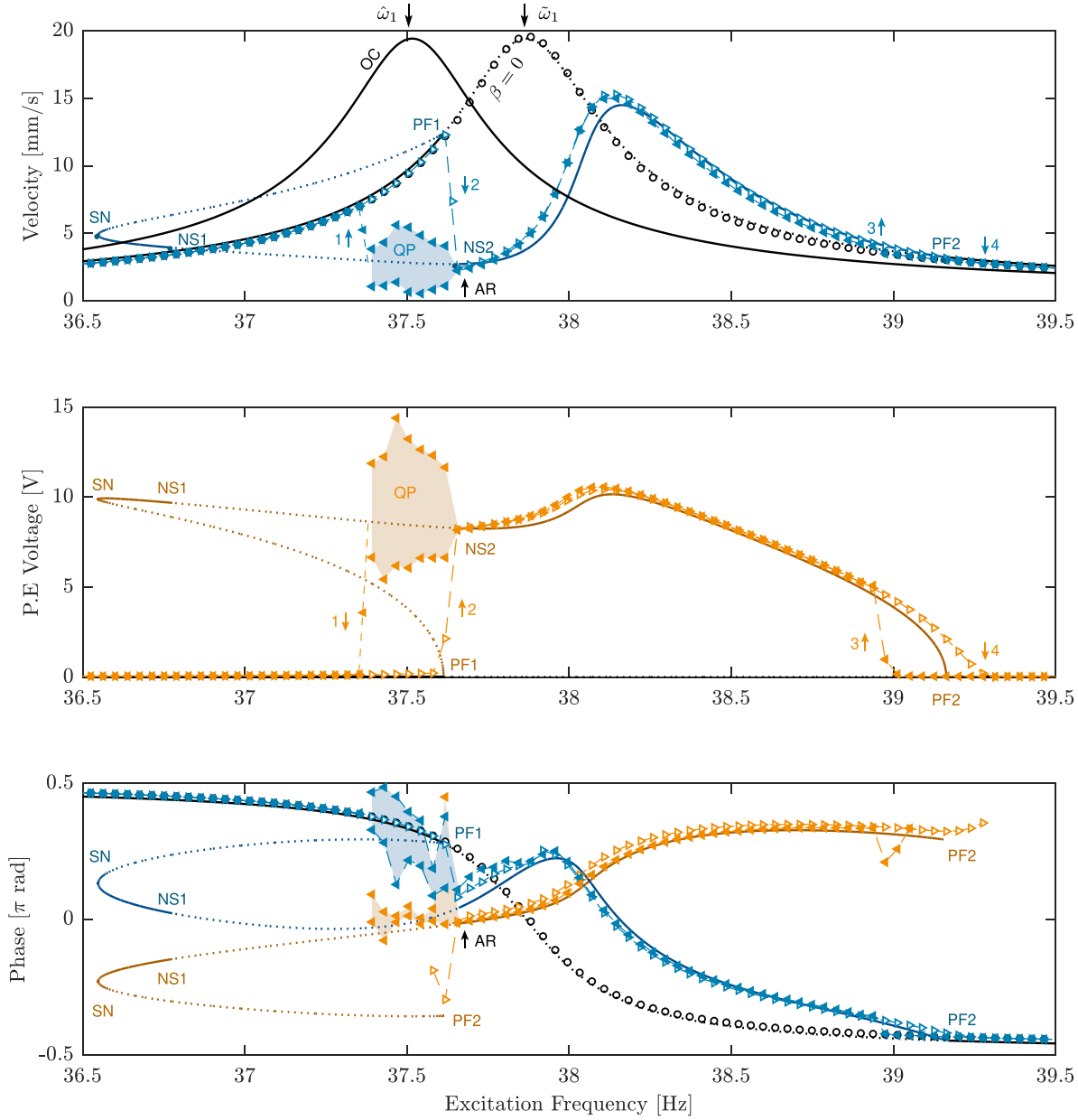

Figure 10. Experimental and numerical results comparison of the amplitudes of v_{H1} and $V_{H1/2}$ and the phase angles ϕ_v and ϕ_V, plotted in blue and orange, respectively. The results are estimated with $F = 0.45$ mN, $\xi_e = 0.002$, $\xi_1 = 0.005$, $\beta = 0.035$, and $r_1 = 0.537$. The numerical data are shown in solid and dotted lines for stable and unstable solutions, respectively, in dark blue and orange, with the uncoupled solution plotted in black. The experimental data are plotted respectively with $-\triangleright-$ and $-\blacktriangleleft-$ for sweeping up and down in the excitation frequency Ω. The experimental uncoupled results are shown in $-\circ-$. The experimental and numerical quasi-periodic regime are shown in the shaded region and the dashed-dotted line, respectively.

signal ($n_1 = n_{1/2} = 12$ in practice). Moreover, at each excitation frequency Ω, the averages of equation (29) were evaluated for ten successive $n_k T_k$ time blocks, to identify quasi-periodic regimes.

This procedure enable to robustly estimate v_{H1}, φ_v, $V_{\mathrm{H1/2}}$ and φ_V, in order to obtain u_{H1}, $Q_{\mathrm{H1/2}}$ and γ_1 using equations (23), (25) and (27):

$$u_{\mathrm{H1}} = v_{\mathrm{H1}}/\Omega, \quad Q_{\mathrm{H1/2}} = C_{\mathrm{pi}} V_{\mathrm{H1/2}}, \quad \gamma_1 = 2\varphi_V - \varphi_v - \frac{\pi}{2}. \tag{32}$$

4. Experimental results

4.1. Experimental validation of the theoretical predictions

As an initial step, we compared the numerical results of the system (2*a*) and (2*b*), integrated with Manlab, to the experimental results. This is shown in figure 10, where the numerical and experimental frequency responses are plotted for the amplitudes of v_{H1} and $V_{H1/2}$, in addition to the phase angles φ_v and φ_V. The measurements were done to catch the whole response features by sweeping up and down the

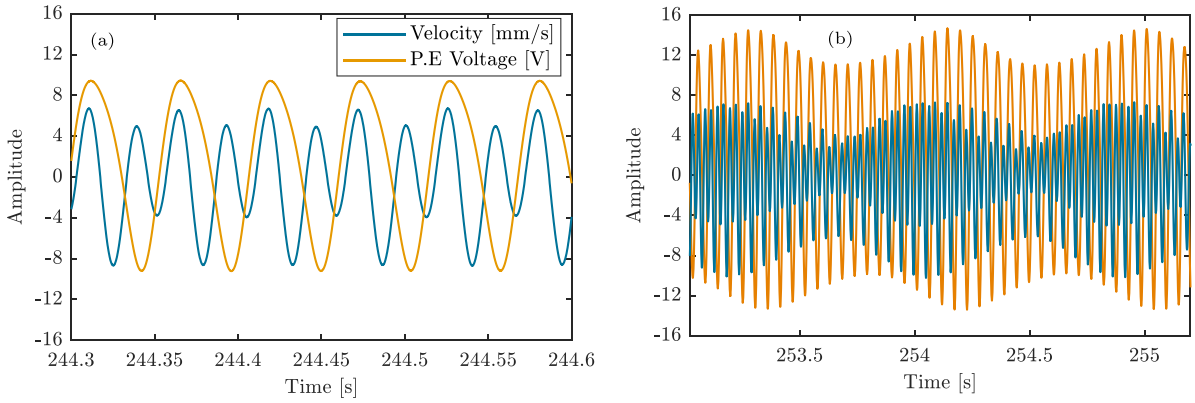

Figure 11. Experimental time signals of $v(t)$ and $V(t)$ for two frequency points in figure 10: (left) the periodic response at $\Omega = 37.75$ Hz and (right) the QP regime at $\Omega = 37.5$ Hz.

excitation frequency. Then, the amplitude and the phases are extracted at each frequency using the demodulation procedure discussed in section 3.4. The comparison between the numerical and experimental results is illustrated as follows.

One can first observe that two linear responses are plotted in black. The first corresponds to the response in the open circuit (OC) case, while the other one corresponds to the linear response when connecting only the R-L version of the full shunt circuit shown in figure 8 (i.e. with $\beta = 0$). The latter case is compared with the experimental results showing an excellent agreement, validating the estimated electromechanical modal parameters of section 3.2. Also, the latter case admits a resonance frequency $\tilde{\omega}_1$ slightly higher than the open circuit frequency $\hat{\omega}_1$ due to the coupling effect, as discussed in section 2.3.

Then the experimental and numerical nonlinear frequency responses of the velocity and voltage show a very good overall agreement. Namely, the energy transfer from the H1 harmonic (at Ω) to the H1/2 harmonic (at $\Omega/2$) due to the 2:1 internal resonance is experimentally observed. The main features obtained theoretically in figure 4 are experimentally validated. Namely, the antiresonance (at point AR, $\Omega/(2\pi) = 37.72$ Hz) is clearly observed, especially in the sweeping-down response. Although the value of r_1 is chosen to have $\omega_2 = 2\omega_1$, the antiresonance is shifted from the resonance frequency (to the lower frequencies), due to the non-resonant terms, as predicted numerically. One can realize that the bifurcation topology of the numerical solution is also validated experimentally, especially for the pitchfork bifurcation PF1, which is predicted at the same frequency as the experimental jump 2. However, a small difference is seen for the other pitchfork bifurcation (PF2), for which the theory suggests that jumps 3 and 4 should appear at the same frequency. The numerically predicted quasi-periodic (QP) solution is also seen experimentally near the antiresonance, only for the sweeping down case. It appears exactly at point NS2, as predicted by the change of stability of the theoretical branch. However, the QP frequency range is smaller in experiments since it stops at jump 1 in the sweep-down response, for which the response jumps back to the uncoupled response. In theory, the end of the QP response is predicted at point NS1 in the low frequencies. This difference could result from an instability in the QP solution (which cannot be predicted by Manlab). A more detailed stability analysis could be necessary to ensure this, which is beyond the scope of this work.

The numerical and experimental responses of the phase angles φ_v and φ_V also show a good agreement. Note that φ_V is only shown in the frequency range where the energy transfer occurs (i.e. between jumps 1 and 4). At the antiresonance (at point AR, $\Omega/(2\pi) = 37.72$ Hz), $\varphi_V = -0.01\ \pi$ rad and $\varphi_v = 0.05\pi$ rad. Thus, using equation (32), γ_1 is estimated to $-0.57\pi \approx 3\ \pi/2$ rad, validating the feature seen theoretically in figure 4.

To extend the above analysis, figure 11 displays two examples of measured time signals. Figure 11(a) shows a periodic response (around $\Omega/(2\pi) = 37.75$ Hz), in which one can clearly observe the H1 and H1/2 harmonics superposition in the time signals, validating equation (14). Moreover, because this periodic response was chosen near the antiresonance, the H1 harmonic amplitude is small and the effect of the H1/2 harmonic, related to the nonlinear shunt, is significantly large. Figure 11(b) shows a QP solution (at $\Omega/(2\pi) = 37.5$ Hz), for which the beatings are clearly visible.

From the above analysis, one can conclude that the agreement between experiments and theory is remarkable and that all theoretical features of the nonlinear shunt are recovered experimentally: the bifurcation scenario, the nonlinear antiresonance, the locking of γ_1 at $3\pi/2$ and the existence of a QP solution.

4.2. *Effect of the nonlinearity gain* β

As illustrated in the theoretical results of [1], the nonlinear gain β has a crucial effect on the absorber performance. We measured the amplitudes v_{H1} and $V_{H1/2}$ for three different values of β, as shown in figure 12, by sweeping up and down in the excitation frequency. Note that the value of β was modified by changing the value of resistance R_8 in the shunt circuit (see equation (20)).

The main advantage of increasing the value of β on the absorber performance is the antiresonance amplitude reduction (at points AR1, AR2, and AR3), which is clearly

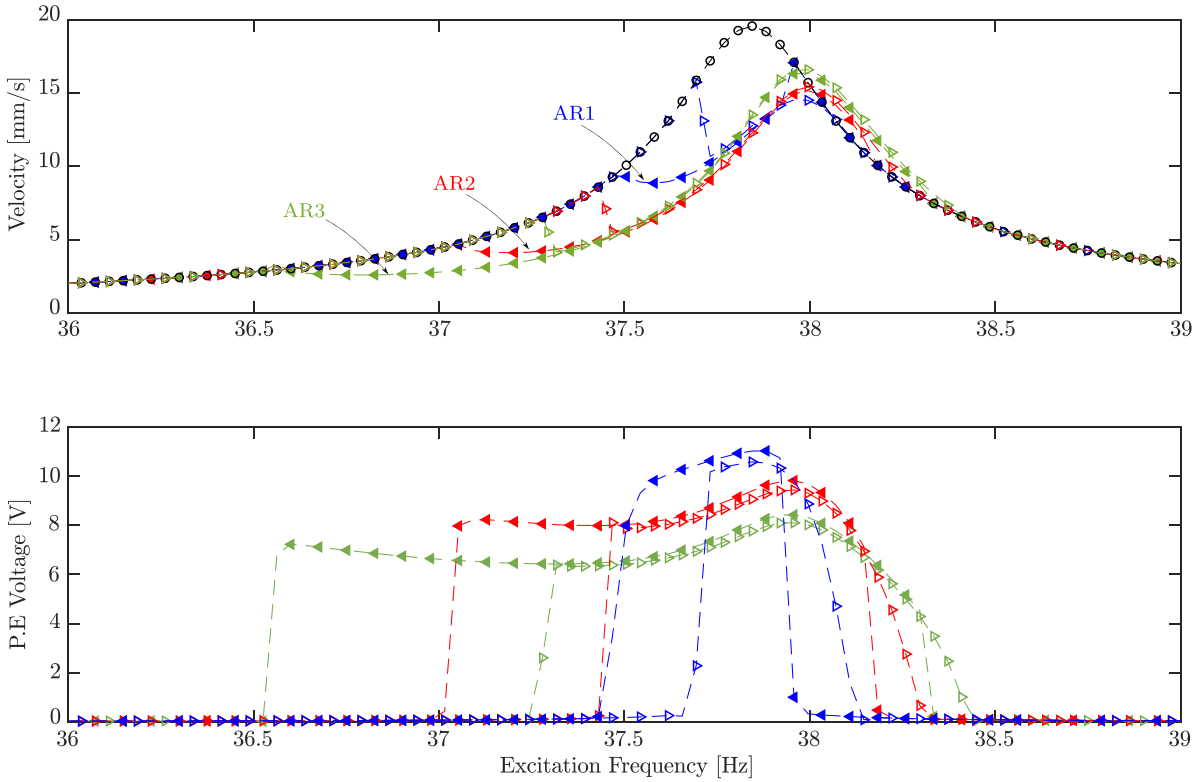

Figure 12. Experimental results for v_{H1} and $V_{H1/2}$ for different values of β. The values of β for the blue, red, and dark green curves are respectively 0.012, 0.023, and 0.035. The tests are done with $F = 0.45$ mN, $\xi_e = 0.002$, $\xi_1 = 0.005$, and $r_1 = 0.524$. The experimental data are plotted respectively with $-\triangleright-$ and $-\blacktriangleleft-$ for sweeping up and down in the excitation frequency Ω. The experimental uncoupled results are shown in $-\circ-$.

observed. However, it appears in parallel to an antiresonance frequency shift, as predicted by theory. This drawback can be counter-balanced by a detuning of the electrical oscillator, as illustrated in section 4.4.

The other advantage of increasing β is the reduction of the PE voltage amplitude, which could be interesting to remain in the functioning limits of the electrical components of the circuit. Another drawback of increasing β is the amplitude amplification of the peak to the right of the linear resonance, which reduces the usable frequency range of the absorber.

4.3. Effect of the excitation level

The effect of the excitation level on the response is illustrated in figure 13, where only downward frequency sweeps are shown. The ratio r_1 is also chosen to have $\omega_1/\omega_2 \simeq 0.5$ and activate the internal resonance, using figure 2 to take into account the effect of the piezoelectric coupling. One can realize that increasing the excitation amplitude while keeping the other design parameters fixed leads to increased velocity and PE patch voltage amplitudes. Also, the peak's amplitude observed to the right of the linear resonance peak in the velocity response increases with the excitation level (analogous to the effect of β). Moreover, a softening behavior can be seen when looking at the voltage response for $F_0 = 2.5$ mN. A QP regime is detected at $F_0 = 0.45$ mN and $F_0 = 1.3$ mN near the antiresonance.

Looking at the antiresonance, one can observe that its amplitude remains almost constant with the increase of the excitation level, but shifts to the lower frequencies as the excitation level increases. This validates the numerical predictions in figure 4, suggesting a violation of the saturation phenomenon at a fixed excitation frequency.

4.4. Saturation phenomenon with detuning

Our purpose is to preserve the saturation phenomenon to enhance the absorber's efficiency. Because the antiresonance amplitude remains constant, it is sufficient to lock the antiresonance at the resonance frequency. This is done following the antiresonance (AR) correction described in section 2.4. Namely, a change in the tuning parameter r_1 should be introduced for each excitation level by changing the inductance in the shunt circuit.

The procedure to track the antiresonance and then lock it at a prescribed frequency is established before performing the stepped sine measurements. Namely, a sinusoidal signal of frequency equal to the mechanical resonance frequency $\tilde{\omega}_1/(2\pi) = 37.75$ Hz is amplified to the desired excitation level and then fed to the coil. This resonance frequency is the one measured with $\beta = 0$ as in figure 13. After reaching the steady-state with the nonlinear subharmonic energy transfer, the velocity $v(t)$ and the PE patch voltage $V(t)$ are visualized using an oscilloscope in an XY mode to obtain a Lissajous plot (i.e.

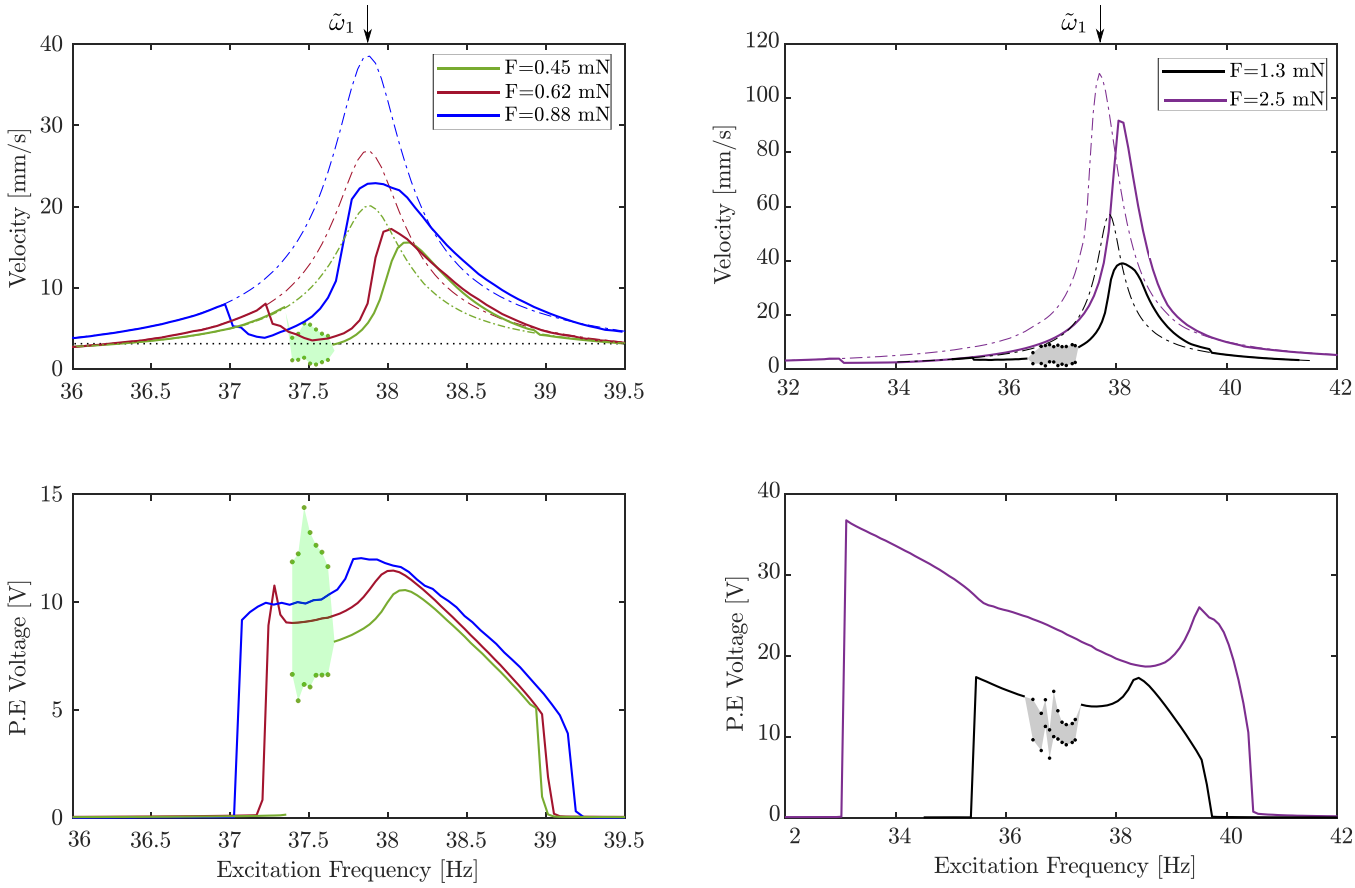

Figure 13. Experimental results of v_{H1} (first row) and $V_{H1/2}$ (second row) for several excitation levels F with unit of mN. Only the data for sweeping down the excitation frequency are shown in solid lines. The measurements are done for $\beta = 0.035$, $\xi_e = 0.002$, $\xi_1 = 0.005$, and $r_1 = 0.537$. The shaded regions depict the detected quasi-periodic regime.

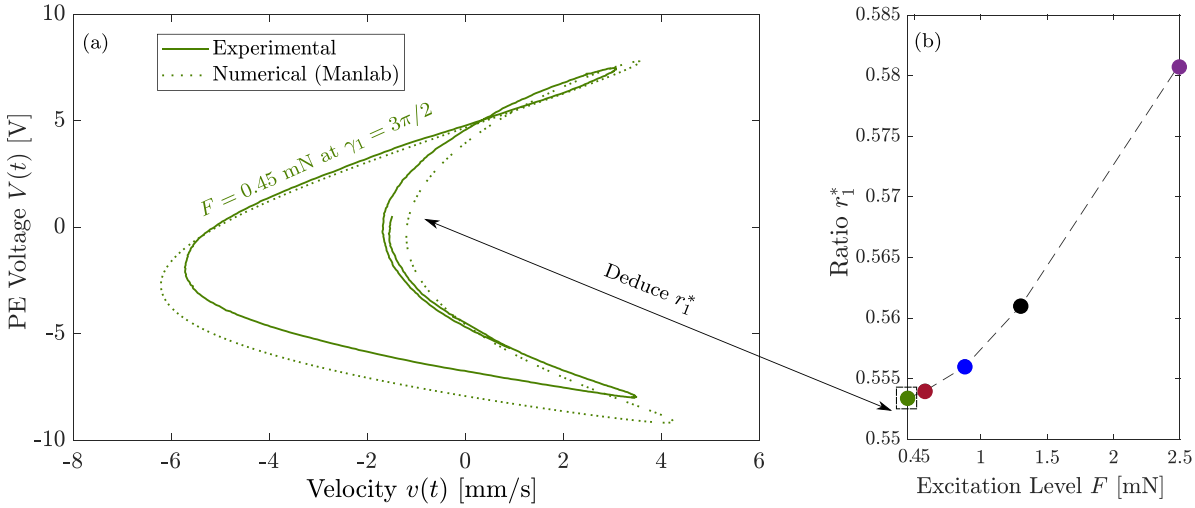

Figure 14. (a) Example of Lissajous plot for $F = 0.45$ mN estimated numerically (with Manlab) and experimentally. (b) Deduced value of r_1^* for different excitation levels. The curves are estimated for $\beta = 0.035$, $\xi_e = 0.002$, and $\xi_1 = 0.005$.

the voltage as a function of the velocity). Because of the fixed value of the phase angle $\gamma_1 = 3\pi/2$, a *unique shape* for the Lissajous plot appears when the antiresonance is shifted to the resonance frequency. In other words, we vary the inductance value until getting the numerically predicted Lissajous plot for $\gamma_1 = 3\pi/2$ as shown in figure 14(a). Thus, the achieved inductance value is the required one to have the proper ratio r_1 (denoted by r_1^*) to lock the antiresonance at the resonance frequency $\tilde{\omega}_1$. The same procedure is repeated for each excitation level, enabling us to have an $r_1^* = f(F_0)$ relation, as

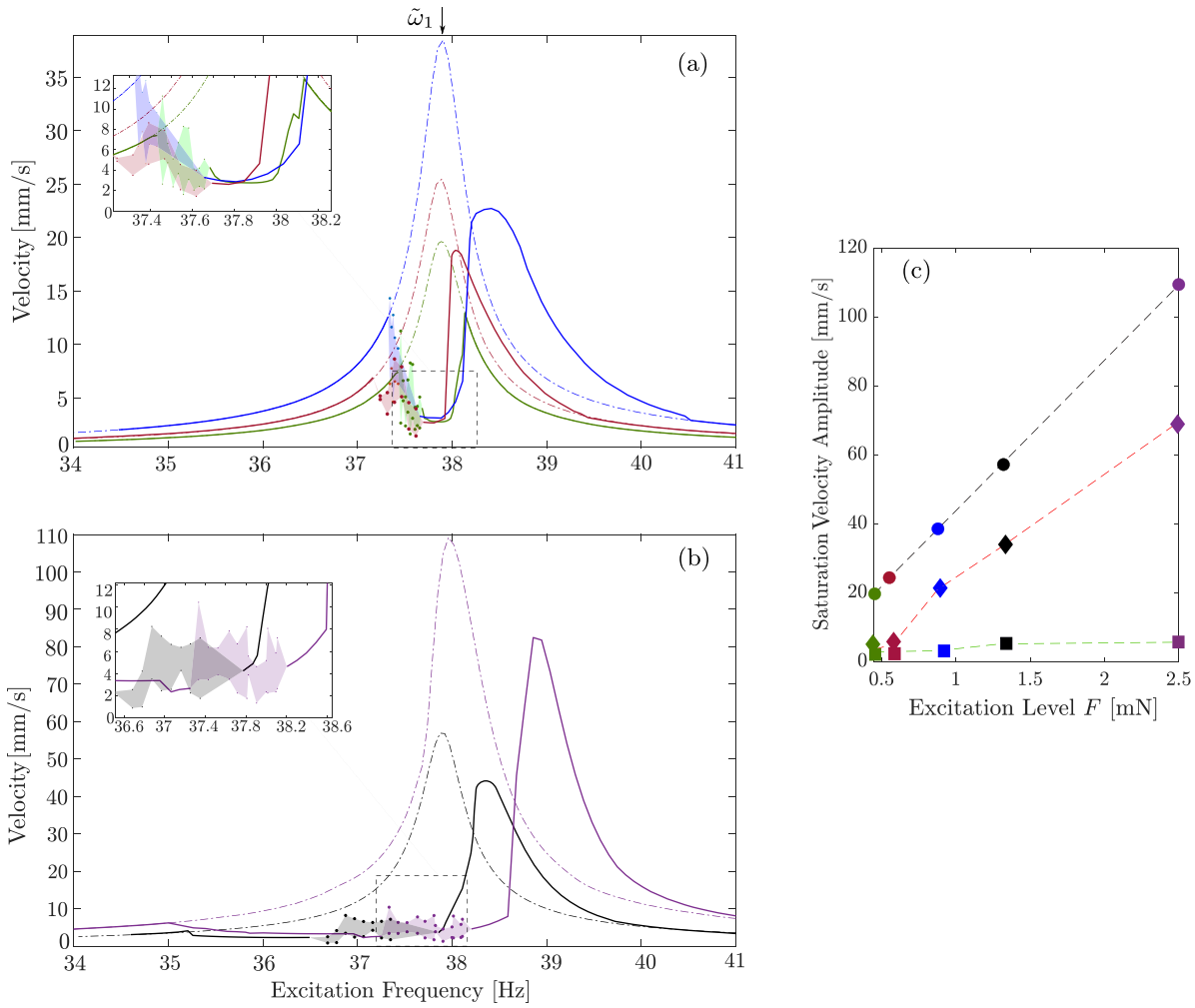

Figure 15. Experimental frequency response of v_{H1} for sweeping down the excitation frequency for several excitation levels with the AR correction. (a) The response for $F = 0.45$ mN (in green), $F = 0.58$ mN (in dark red), and $F = 0.88$ mN (in blue). (b) The response for $F = 1.3$ mN (in black), $F = 2.5$ mN (in purple). (c) Antiresonance saturation amplitude v^*_{H1} at the resonance frequency $\tilde{\omega}_1$ versus the excitation level plotted for three different cases: the linear response, with fixed $r_1 = 0.537$, and with the AR correction in. The curves are estimated for $\beta = 0.035$, $\xi_e = 0.002$, and $\xi_1 = 0.0055$. The shaded regions depict the detected quasi-periodic regime.

plotted in figure 14(b). For example, this relation shows that r_1^*, for $F = 0.45$ mN and $\beta = 0.035$, should be 0.547. Also, this relation suggests that a further decrease in the inductance (i.e. an increase in r_1) should be introduced as the excitation level increases to lock the antiresonance. Note that this relation depends on the other design parameters (i.e. β, k_1).

The frequency response of v_{H1} is experimentally measured by setting the proper value of r_1 using the $r_1^* = f(F_0)$ relation of figure 14(b). The results are illustrated in figures 15(a) and (b) by sweeping down the excitation frequency for the same excitation levels used in figure 13. One can note that using the suggested AR correction, the antiresonance is locked at the prescribed frequency (i.e. at $\tilde{\omega}_1/(2\pi) = 37.75$ Hz), leading to the preserving of the saturation phenomenon. However, changing the value of r_1 led to the appearance of QP regimes near the antiresonance that were not appearing in figure 13 for constant r_1, for example in the response for $F = 0.88$ mN. Also, one can note a slightly softening behavior on the uncoupled resonance curve in the case of the highest forcing level (in purple), which could be due to the non-negligible effects of the material piezoelectric nonlinearities in the PE patches [42]. In addition, for the highest excitation level, the QP regime being shifted further to the left made the Lissajous plot more complicated to obtain at the resonance frequency 37.75 Hz; we obtained r_1^* for a slightly higher frequency to have the periodic solution.

Note that the linear responses shown in figures 15(a) and (b) are plotted by setting $\beta = 0$ with values of r_1 equal to r_1^* which varies for each excitation level (unlike figure 4 where a constant value of r_1 is used). Based on this, the resonance frequency increases slightly above $\tilde{\omega}_1$ as the excitation level increases. This can be observed at the highest excitation that requires the highest value of r_1^*. In this context, the suggested AR correction locks the antiresonance at a unique prescribed frequency that is slightly lower than the resulting linear resonance frequency for higher excitation levels, due to its dependency on r_1.

To further illustrate the saturation phenomenon, the amplitude of v_{H1} at the prescribed frequency $\tilde{\omega}_1$, denoted by v^*_{H1},

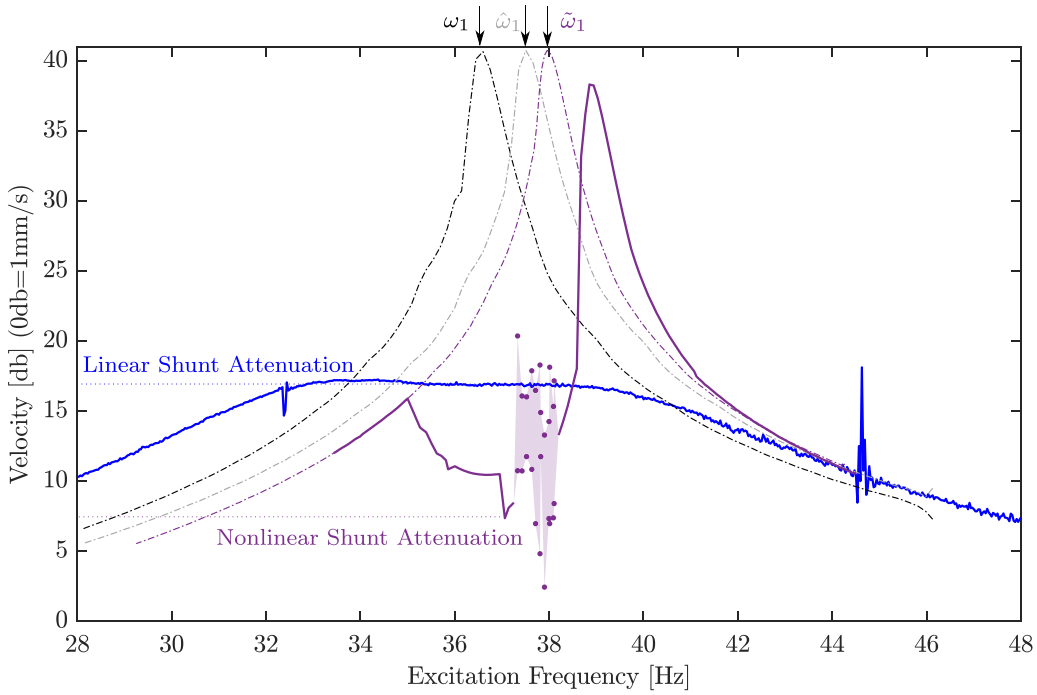

Figure 16. Comparison between the performance of the optimized linear shunt and the designed absorber for $F = 2.5$ mN, $\beta = 0.035$, and $\xi_1 = 0.0055$. The dashed curves depict the linear responses for the short circuit case (black), the open circuit case (brown) and $\beta = 0$ (purple). The solid lines depict the responses for $\beta = 0.035$ (purple) and for the optimized linear shunt (blue).

is plotted versus the excitation level F in figure 15(c) (similar to figure 5(b)). The amplitudes of v_{H1}^* are taken directly from the experimental measurements showing the frequency response of v_{H1}. Three different cases are plotted: the linear case ($\beta = 0$), the case where a constant r_1 is used (see figure 13), and the case when introducing the antiresonance correction (figures 15(a) and (b)). The results suggest a significant attenuation enhancement for the latter case where the saturation phenomenon is *almost* preserved. As a matter of fact, one can observe a slight increase in v_{H1}^* when using the AR correction mainly because of the slight increase of the electrical damping ξ_e due the increasing value of r_1^* for higher excitation levels.

4.5. Performance comparison with optimized linear shunt

To further demonstrate the nonlinear shunt performance, figure 16 shows a comparison of the resonant response of the structure with the nonlinear shunt for the highest excitation level $F = 2.5$ mN (purple curve of figure 15) and with a tuned linear resonant (RL) shunt. For the latter, $\beta = 0$ and the electrical frequency $\omega_e \simeq \hat{\omega}_1$ was tuned with the equal peak method [6] (with $R_e = 35.26$ kΩ and $L = 555.82$ H, with $R_4 = 27.79$ kΩ).

5. Conclusion

In this paper, the experimental validation of a passive nonlinear piezoelectric shunt absorber, introduced theoretically in our previous study [1], was performed. This absorber is designed by intentionally introducing a quadratic nonlinearity proportional to the square of the voltage across the piezoelectric patches (PE patches) in series with a resonant shunt circuit. Doing so creates a 2:1 internal resonance between a given mechanical mode of the primary structure and the shunt circuit tuned at the first subharmonic frequency. Our designed absorber aims to exploit the convenient features of such an internal resonance: a *saturation phenomenon*, in which the amplitude of the mechanical mode becomes independent of the excitation amplitude after a threshold, and a *nonlinear antiresonance* in place of the linear resonance frequency, leading to high vibration attenuation. These two features are linked to the nonlinear energy transfer from the mechanical mode to be attenuated to the electrical mode characterized by the shunt circuit.

We showed a remarkable agreement between our experiments and the theoretical prediction, thus perfectly validating them. In addition, the performances of the shunt were explored, showing an amplitude that is independent of the vibration level at the antiresonance, associated with better performance at high amplitude than a classical linear resonant shunt. One drawback of our architecture, based on a nonlinear voltage proportional to the square of the piezoelectric (PE) voltage, is the unexpected detuning of the shunt as a function of the amplitude, that was manually corrected by a phase-locking of the PE voltage with the mechanical response of the structure. Another drawback is the saturation limit of the analog electronic components, which limits the maximum amplitude of operation of the shunt and constraints the design of the electronic circuit, to finely balance the voltages and avoid noise in the circuit.

Data availability statement

All data that support the findings of this study are included within the article (and any supplementary files).

Aknowledgments

The Région Hauts de France and the Carnot ARTS Institute are warmly thanked for the PhD grant of the first author.

ORCID iDs

Zein Alabidin Shami https://orcid.org/0000-0002-5470-4957
Christophe Giraud-Audine https://orcid.org/0000-0003-3461-0328
Olivier Thomas https://orcid.org/0000-0001-7240-5259

References

[1] Shami Z A, Giraud Audine C and Thomas O 2022 A nonlinear piezoelectric shunt absorber with a 2:1 internal resonance: theory *Mech. Syst. Signal Process.* (https://doi.org/10.1016/j.ymssp.2021.108768) In press

[2] Lanchester F W 1914 Damping torsional vibrations in crank shafts *US Patent* No 1085443

[3] Frahm H 1911 Device for damping vibrations of bodies *US Patent* No 989958

[4] Hagood N and Von Flotow A 1991 Damping of structural vibrations with piezoelectric materials and passive electrical networks *J. Sound Vib.* **146** 243–68

[5] Auleley M, Thomas O, Giraud-Audine C and Mahé H 2021 Enhancement of a dynamic vibration absorber by means of an electromagnetic shunt *J. Intell. Mater. Syst. Struct.* **32** 331–54

[6] Thomas O, Ducarne J and Deü J-F 2012 Performance of piezoelectric shunts for vibration reduction *Smart Mater. Struct.* **21** 015008

[7] Berardengo M, Thomas O, Giraud-Audine C and Manzoni S 2016 Improved resistive shunt by means of negative capacitance: new circuit, performances and multi-mode control *Smart Mater. Struct.* **25** 075033

[8] Berardengo M, Manzoni S, Thomas O and Vanali M 2021 Guidelines for the layout and tuning of piezoelectric resonant shunt with negative capacitances in terms of dynamic compliance, mobility and accelerance *J. Intell. Mater. Syst. Struct.* **32** 2092–107

[9] Auleley M, Giraud-Audine C, Mahé H and Thomas O 2021 Tunable electromagnetic resonant shunt using pulse-width modulation *J. Sound Vib.* **500** 116018

[10] Darleux R, Lossouarn B and Deü J-F 2020 Broadband vibration damping of non-periodic plates by piezoelectric coupling to their electrical analogues *Smart Mater. Struct.* **29** 054001

[11] Gripp J and Rade D 2018 Vibration and noise control using shunted piezoelectric transducers: a review *Mech. Syst. Signal Process.* **112** 359–83

[12] Shivashankar P and Gopalakrishnan S 2020 Review on the use of piezoelectric materials for active vibration, noise and flow control *Smart Mater. Struct.* **29** 053001

[13] Gatti G, Brennan M and Tang B 2019 Some diverse examples of exploiting the beneficial effects of geometric stiffness nonlinearity *Mech. Syst. Signal Process.* **125** 4–20

[14] Ledezma-Ramirez D F, Tapia-González P E, Ferguson N, Brennan M J and Tang B 2019 Recent advances in shock vibration isolation: an overview and future possibilities *Appl. Mech. Rev.* **71** 060802

[15] Silva T M, Clementino M A, De Marqui C and Erturk A 2018 An experimentally validated piezoelectric nonlinear energy sink for wideband vibration attenuation *J. Sound Vib.* **437** 68–78

[16] Zhao G, Raze G, Paknejad A, Deraemaeker A, Kerschen G and Collette C 2020 Active nonlinear energy sink using force feedback under transient regime *Nonlinear Dyn.* **102** 1319–36

[17] Habib G, Detroux T, Viguié R and Kerschen G 2015 Nonlinear generalization of Den Hartog's equal-peak method *Mech. Syst. Signal Process.* **52–53** 17–28

[18] Soltani P and Kerschen G 2015 The nonlinear piezoelectric tuned vibration absorber *Smart Mater. Struct.* **24** 075015

[19] Lossouarn B, Deü J-F and Kerschen G 2018 A fully passive nonlinear piezoelectric vibration absorber *Phil. Trans. R. Soc.* A **376** 20170142

[20] Raze G, Jadoul A, Guichaux S, Broun V and Kerschen G 2019 A digital nonlinear piezoelectric tuned vibration absorber *Smart Mater. Struct.* **29** 015007

[21] Lossouarn B, Kerschen G and Deü J-F 2021 An analogue twin for piezoelectric vibration damping of multiple nonlinear resonances *J. Sound Vib.* **511** 116323

[22] Clark W W 2000 Vibration control with state-switched piezoelectric materials *J. Intell. Mater. Syst. Struct.* **11** 263–71

[23] Richard C, Guyomar D, Audigier D and Ching G 1999 Semi-passive damping using continuous switching of a piezoelectric device *Proc. of SPIE Smart Structures and Conf.: Passive Damping and Isolation* vol 3672 pp 104–11

[24] Oueini S and Golnaraghi M 1996 Experimental implementation of the internal resonance control strategy *J. Sound Vib.* **191** 377–96

[25] Oueini S S, Nayfeh A H and Golnaraghi M F 1997 A theoretical and experimental implementation of a control method based on saturation *Nonlinear Dyn.* **13** 189–202

[26] Oueini S S, Nayfeh A H and Pratt J R 1998 A nonlinear vibration absorber for flexible structures *Nonlinear Dyn.* **15** 259–82

[27] Pai P, Wen B, Naser A and Schulz M 1998 Structural vibration control using pzt patches and non-linear phenomena *J. Sound Vib.* **215** 273–96

[28] Pai P F, Rommel B and Schulz M J 2000 Dynamics regulation of a skew cantilever plate using PZT patches and saturation phenomenon *J. Intell. Mater. Syst. Struct.* **11** 642–55

[29] 1988 IEEE Standard on Piezoelectricity *ANSI/IEEE Std 176-1987* (https://doi.org/10.1109/IEEESTD.1988.79638)

[30] Géradin M and Rixen D 2015 *Mechanical Vibrations* 3rd edn (New York: Wiley)

[31] Nayfeh A H and Mook D T 1979 *Nonlinear Oscillations* (New-York: Wiley)

[32] Monteil M, Touzé C, Thomas O and Benacchio S 2014 Nonlinear forced vibrations of thin structures with tuned eigenfrequencies: the cases of 1:2:4 and 1:2:2 internal resonances *Nonlinear Dyn.* **75** 175–200

[33] Touzé C, Thomas O and Chaigne A 2004 Hardening/softening behaviour in non-linear oscillations of structural systems using non-linear normal modes *J. Sound Vib.* **273** 77–101

[34] Touzé C, Vizzaccaro A and Thomas O 2021 Model order reduction methods for geometrically nonlinear structures: a review of nonlinear techniques *Nonlinear Dyn.* **105** 1141–90

[35] Guillot L, Cochelin B and Vergez C 2019 A Taylor series-based continuation method for solutions of dynamical systems *Nonlinear Dyn.* **98** 2827–45

[36] Guillot L, Lazarus A, Thomas O, Vergez C and Cochelin B 2020 A purely frequency based Floquet-Hill formulation for

the efficient stability computation of periodic solutions of ordinary differential systems *J. Comput. Phys.* **416** 109477
[37] Ducarne J, Thomas O and Deü J-F 2012 Placement and dimension optimization of shunted piezoelectric patches for vibration reduction *J. Sound Vib.* **331** 3286–303
[38] Thomas O, Touzé C and Chaigne A 2003 Asymmetric non-linear forced vibrations of free-edge circular plates, part 2: experiments *J. Sound Vib.* **265** 1075–101
[39] Antoniou A 1969 Realisation of gyrators using operational amplifiers and their use in RC-active-network synthesis *Proc. Inst. Electr. Eng.* **116** 13
[40] Yuce E and Minaei S 2009 On the realization of simulated inductors with reduced parasitic impedance effects *Circuits Syst. Signal Process.* **28** 451–65
[41] Colin M, Thomas O, Grondel S and Cattan E 2020 Very large amplitude vibrations of flexible structures: experimental identification and validation of a quadratic drag damping model *J. Fluids Struct.* **97** 103056
[42] Givois A, Giraud-Audine C, Deü J-F and Thomas O 2020 Experimental analysis of nonlinear resonances in piezoelectric plates with geometric nonlinearities *Nonlinear Dyn.* **102** 1451–62